Synchrotron JSR JOURNAL OF SYNCHROTRON RADIATION

ISSN 1600-5775

Received 31 October 2018
Accepted 21 June 2019

Edited by D. A. Reis, SLAC National Accelerator Laboratory, USA

Keywords: XFELs; self-seeding; channel-cut crystals.

A micro channel-cut crystal X-ray monochromator for a self-seeded hard X-ray free-electron laser

Taito Osaka,[a]* Ichiro Inoue,[a] Ryota Kinjo,[a] Takashi Hirano,[b] Yuki Morioka,[b] Yasuhisa Sano,[b] Kazuto Yamauchi[b] and Makina Yabashi[a,c]

[a]RIKEN SPring-8 Center, 1-1-1 Kouto, Sayo-cho, Sayo-gun, Hyogo 679-5148, Japan, [b]Department of Precision Science and Technology, Graduate School of Engineering, Osaka University, 2-1 Yamada-oka, Suita, Osaka 565-0871, Japan, and [c]JASRI, 1-1-1 Kouto, Sayo-cho, Sayo-gun, Hyogo 679-5198, Japan. *Correspondence e-mail: osaka@spring8.or.jp

A channel-cut Si(111) crystal with a channel width of 90 µm was developed for achieving reflection self-seeding in hard X-ray free-electron lasers (XFELs). With the crystal a monochromatic seed pulse is produced from a broadband XFEL pulse generated in the first undulator section with an optical delay of 119 fs at 10 keV. The small optical delay allows a temporal overlap between the seed optical pulse and the electron bunch by using a small magnetic chicane for the electron beam placed between two undulator sections. Peak reflectivity reached 67%, which is reasonable compared with the theoretical value of 81%. By using this monochromator, a monochromatic seed pulse without broadband background in the spectrum was obtained at SACLA with a conversion efficiency from a broadband XFEL pulse of 2×10^{-2}, which is ∼10 times higher than the theoretical efficiency of transmission self-seeding using a thin diamond (400) monochromator.

1. Introduction

X-ray free-electron lasers (XFELs) operating in the self-amplified spontaneous emission (SASE) scheme (Kondratenko & Saldin, 1980; Bonifacio *et al.*, 1984) have generated hard X-ray beams with unique characteristics, such as ultra-high peak power, nearly full transverse coherence and ultra-short pulse duration at the femtosecond level (Huang & Kim, 2007). In the SASE scheme, spontaneous radiation emitted from an electron bunch with a random statistical modulation of the beam density is amplified while propagating through a periodic magnetic field in long undulators. However, the stochastic nature causes poor longitudinal coherence and a broad spectrum with a relative bandwidth of ∼0.3% (Saldin *et al.*, 1999). A monochromator is widely used to monochromatize SASE-XFEL pulses, whereas the photon flux is decreased considerably by a factor of ∼30.

To generate intense and narrowband XFEL pulses in the hard X-ray regime, a self-seeding scheme has been proposed (Feldhaus *et al.*, 1997). In this scheme, a monochromator is placed in the middle of a magnetic chicane of the electron bunch, which separates the undulators into two sections. A monochromatic seed pulse is produced from a broadband SASE-XFEL pulse generated in the first undulator section through the monochromator. At the same time, the electron bunch is detoured in the magnetic chicane and then spatio-temporally overlapped with the seed pulse downstream of the chicane. Finally, the seed pulse is amplified in the second undulator section while interacting with the electron bunch. The technical difficulty in self-seeding is to assure a temporal

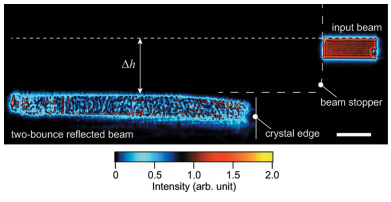

overlap between the electron bunch and the seed pulse. This is because a delay for multi-GeV electron beams is typically limited up to a few hundreds of femtoseconds with a chicane of ∼5 m length, whereas an optical delay is as large as several picoseconds with a conventional Si(111) double-crystal monochromator (DCM) that has a distance between the crystals of several millimetres. Amann *et al.* (2012) demonstrated self-seeding in the hard X-ray regime at the Linac Coherent Light Source (LCLS) (Emma *et al.*, 2010) with a thin diamond (400) monochromator operating in the forward Bragg diffraction geometry. They used a monochromatic pulse echo as a seeding source that follows a prompt SASE-XFEL pulse with an interval of tens of femtoseconds (Geloni *et al.*, 2010, 2011; Lindberg & Shvyd'ko, 2012) and successfully generated a narrowband XFEL beam. With the 'transmission' monochromator, however, the prompt broadband SASE-XFEL pulse propagates through an optical axis common to the seed pulse, preventing accurate characterization of the seed pulse. Furthermore, the conversion efficiency – defined by the ratio of the power of a monochromatic seed pulse to that of an input XFEL pulse – of the transmission monochromator has been theoretically evaluated to be $\sim 2 \times 10^{-3}$ (Lindberg & Shvyd'ko, 2012), being much lower than that of a usual 'reflection' monochromator, which could degrade the electron bunch so as to generate an intense seeding source.

In this paper we report the development of a micro channel-cut monochromator (Bonse & Hart, 1965) as an essential optical component for achieving reflection self-seeding with a high efficiency (Inoue *et al.*, 2019). We designed a channel-cut Si(111) crystal with a channel width of 90 μm, which gives an optical delay as small as ∼100 fs while removing the prompt SASE beam. Since an X-ray beam is reflected twice at the two opposite blades of the channel-cut crystal made of a 'monolithic' single-crystal block, the optical axis of the exit beam is highly stabilized compared with a DCM composed of independent crystals (Diaz *et al.*, 2010). After characterization of the quality of the crystal at a SPring-8 beamline, we performed a feasibility test of the reflection self-seeding at SPring-8 Angstrom Compact free-electron LAser (SACLA) (Ishikawa *et al.*, 2012).

2. Design of the micro channel-cut crystal

To achieve the reflection self-seeding with the micro channel-cut crystal, the following requirements should be satisfied: a small optical delay that is less than the maximum delay for the electron bunch and a large spatial acceptance to receive a major portion of an incident XFEL beam. The delay for the electron bunch Δt_e is approximately given by (Hara *et al.*, 2013)

$$\Delta t_e \simeq \frac{\theta_e^2}{c}\left(L + \frac{2}{3}L_B\right), \tag{1}$$

where θ_e is the deflection angle of the electron beam, c is the speed of light, L is the drift distance between the first and second dipole magnets in the magnetic chicane, and L_B is the length of the magnetic field. The deflection angle can be written as

$$\theta_e \simeq \frac{cBL_B}{E_e}, \tag{2}$$

where B is the magnetic flux density and E_e is the electron beam energy. At SACLA we tune the photon energy of XFEL beams (E_{ph}) by adjusting the electron beam energy E_e and/or the undulator deflection parameter K according to the following relationship,

$$E_{ph} = \frac{2hc}{\lambda_u}\frac{\gamma^2}{1 + K^2/2} \equiv \frac{A\gamma^2}{1 + K^2/2}, \tag{3}$$

where h is Plank's constant, λ_u (= 18 mm) is the undulator periodic length and γ (= E_e/E_{e0}, where E_{e0} is the rest energy of the electron) is the Lorenz factor of the electron beam. The coefficient A (= $2hc/\lambda_u$) is used to simplify the equation. Setting boundary conditions $E_e \le E_{e\_max}$ ($\gamma \le \gamma_{max}$) and $K \le K_{max}$, we have a reference photon energy $E'_{ph} = A\gamma^2_{max}/(1 + K^2_{max}/2)$. For $E_{ph} \le E'_{ph}$, we usually adjust E_e to tune the photon energy E_{ph} with a fixed K of K_{max}, while we change K by fixing $E_e = E_{e\_max}$ for $E_{ph} \ge E'_{ph}$. These conditions give the delay for the electron bunch Δt_e as

$$\Delta t_e \simeq \begin{cases} C\left(B^2/E_{ph}\right) & \text{for } E_{ph} \le E'_{ph}, \\ DB^2 & \text{for } E_{ph} \ge E'_{ph}, \end{cases} \tag{4}$$

with

$$C = \frac{AcL_B^2\left[L + (2/3)L_B\right]}{\left(1 + K_{max}^2/2\right)E_{e0}^2}, \qquad D = \frac{cL_B^2\left[L + (2/3)L_B\right]}{E_{e\_max}^2}. \tag{5}$$

Equation (4) indicates that Δt_e is inversely proportional to E_{ph} for $E_{ph} \le E'_{ph}$, whereas it is independent of E_{ph} for $E_{ph} \ge E'_{ph}$. On the other hand, the optical delay Δt_{ph} for a single channel-cut monochromator in the symmetric case is described by

$$\Delta t_{ph} = \frac{hg}{d_{hkl}E_{ph}}, \tag{6}$$

where g is the channel width of the crystal and d_{hkl} is the lattice spacing for the (hkl) diffraction. In order to introduce the maximum delay Δt_{e_max} to the electron bunch, we apply the maximum magnetic flux density B_{max} to the dipole magnets in the chicane. The upper limit of the width g_{max} is defined such that the optical delay with $g = g_{max}$ is equal to Δt_{e_max}, which can be written as

$$g_{max} = \frac{d_{hkl}}{h}\Delta t_{e\_max}E_{ph} \simeq \begin{cases} C'd_{hkl} & \text{for } E_{ph} \le E'_{ph}, \\ D'd_{hkl}E_{ph} & \text{for } E_{ph} \ge E'_{ph}, \end{cases} \tag{7}$$

with $C' = CB^2_{max}/h$ and $D' = DB^2_{max}/h$. Note that g_{max} is proportional to E_{ph} for $E_{ph} \ge E'_{ph}$; however, it becomes a constant value $C'd_{hkl}$ for $E_{ph} \le E'_{ph}$. it By using a higher order diffraction with a smaller d_{hkl}, the requirement on g becomes more severe, whereas the bandwidth of the seed and the seeded XFEL beam to be achieved could be narrower. The

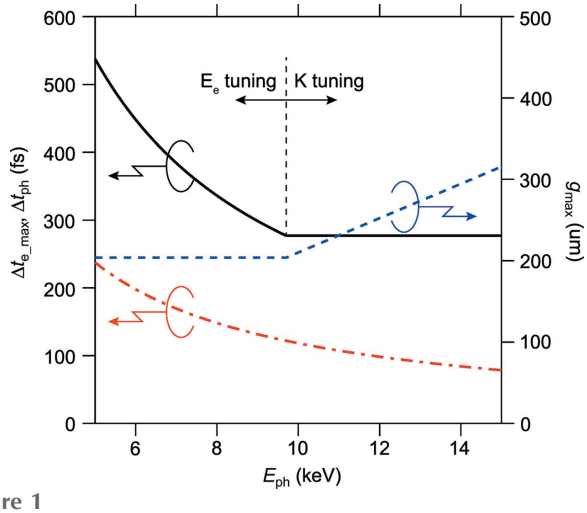

Figure 1
Maximum delay for the electron beam Δt_{e_max} (solid line) introduced with the magnetic chicane at BL3 of SACLA and the corresponding channel width g_{max} (dashed line) as a function of photon energy E_{ph}. The dot-dashed line shows the optical delay imposed by the micro channel-cut monochromator with g = 90 μm.

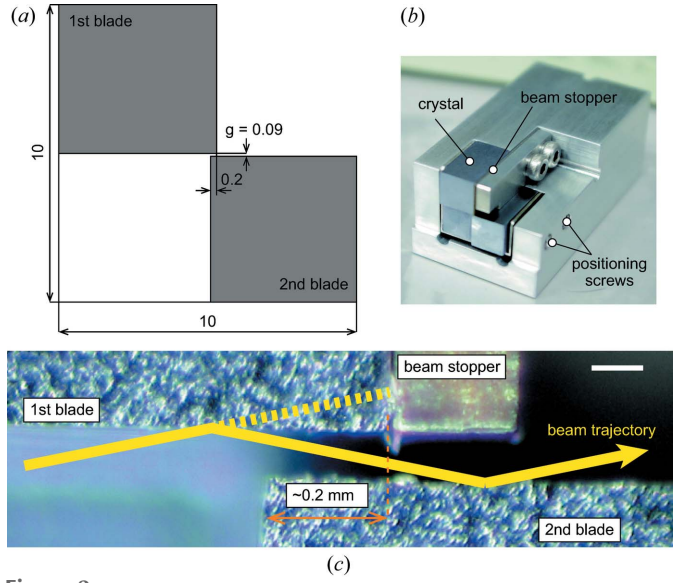

Figure 2
(*a*) Drawing of a micro channel-cut crystal viewed perpendicular to the optical axis (units given in mm). (*b*) Photograph of the crystal mounted on a dedicated holder. X-ray beams propagate from the left to the right. The position of the crystal is finely adjusted by pushing a stainless plate on the crystal from the left, right and bottom sides with screws so as to fit the surface of the first blade to the bottom surface of the beam stopper, as shown in (*c*). (*c*) Optical microscope image of the working area. Scale bar shows 100 μm.

conversion efficiency of the monochromator using a high-order diffraction is also reduced compared with that for a low-order diffraction because of the narrower acceptance in the spectrum.

Fig. 1 shows Δt_{e_max} and the corresponding g_{max} as a function of E_{ph}. Here we used the Si(111) diffraction (d_{111} = 3.136 Å) that is the lowest order diffraction in silicon to achieve a high conversion efficiency, and the latest parameters for the magnetic chicane at SACLA (L = 1.56 m, L_B = 0.34 m and B_{max} = 0.52 T) with boundary conditions E_{e_max} = 7.8 GeV and K_{max} = 2.15. The reference photon energy E'_{ph} is calculated to be 9.69 keV. We concluded that the requirement on the optical delay is satisfied over a wide photon energy range by using a channel-cut Si(111) crystal with $g < C' d_{111}$ = 204 μm. Note that a smaller electron-beam delay is preferred for suppressing unwanted coherent synchrotron radiation and transporting an electron bunch with higher quality into the second undulator section.

For the micro channel-cut crystal the spatial acceptance is considerably limited. The acceptance in the vertical direction is practically as small as g/2 while depending on E_{ph} and the quality of the crystal edge. In the horizontal direction the acceptance is determined by the depth of the diffracting blades, which is typically limited up to 10g because of the difficulty in fabrication of a narrow trench. The size of the XFEL beams at the middle of the magnetic chicane was evaluated to be ∼50 μm full width at half-maximum (FWHM) at 10 keV through a numerical simulation with the FEL simulation code *SIMPLEX* (Tanaka, 2015). Therefore, a spatial acceptance of >50 μm in both directions is needed.

We designed a prototype micro channel-cut crystal, as shown in Fig. 2(*a*), which satisfies all of the above requirements near 10 keV. The channel width g was set to 90 μm, which gives an optical delay of 119 fs at 10 keV, as shown in Fig. 1. The overlap length of the two diffracting blades was designed to be 0.2 mm so as to obtain a spatial acceptance in the vertical direction of at least 50 μm while avoiding the use of an area near the crystal edge. The depth of the channel is ∼0.6 mm, being sufficiently larger than the horizontal beam size. The dimensions of the crystal are 10 mm × 10 mm × 10 mm to facilitate handling of the crystal while the right upper part is removed to place a beam stopper just downstream of the first blade, which is required to block the unwanted transmission beam propagating through the crystal. We note that a single channel-cut monochromator imposes a transverse shift of the beam axis Δh described by

$$\Delta h = 2g \cos\theta_B, \tag{8}$$

where θ_B is the Bragg angle. The shift is less than 180 μm with a micro channel-cut crystal of g = 90 μm, which is acceptable for all the optical components at SACLA. Although the shift can be compensated by using a double channel-cut monochromator operating in the (+, −, −, +) geometry, the optical delay becomes twice as large as that in the single channel-cut monochromator.

The micro channel-cut crystal was made of a floating-zone Si single-crystal block. An ultra-narrow trench with 60–70 μm width and ∼0.6 mm depth was formed with a dicing blade. Then the surface layer of 10–15 μm depth was removed through solution etching. Finally, the working area was moderately polished with fine slurry. Since the channel width of the crystal is one of the most important parameters and difficult to measure with an optical microscope, we accurately characterized the channel width with an X-ray beam using equation (8), as described in Section 3.2.

The crystal was mounted on a dedicated holder [Fig. 2(*b*)] with a beam stopper made of tungsten of 250 µm thickness. The position of the crystal was finely adjusted by positioning screws so as to fit the incident surface to the bottom surface of the beam stopper, as shown in Fig. 2(*c*).

3. Characterization of the micro channel-cut crystal

3.1. Experimental setup

We characterized the micro channel-cut crystal using X-ray reflection topography and rocking curve measurements at the 1 km-long beamline BL29XU of SPring-8 (Tamasaku *et al.*, 2001). A 10 keV X-ray beam emitted from an undulator was monochromated by a SPring-8 standard Si(111) DCM (Yabashi *et al.*, 1999). The size of the X-ray beam was reduced to 500 µm [horizontal (H)] × 50 µm [vertical (V)], with a four-jaw slit located 987 m downstream of the source. The rocking curve was measured with two ion chambers, while the reflection topographs were taken with a high-resolution X-ray camera with a pixel size of 325 nm (Kameshima *et al.*, 2019) placed at ∼1 m downstream of the crystal.

3.2. Results

Fig. 3(*a*) shows a reflection profile under the Bragg condition. Both the incident and reflected beams were observed in the field of view of the camera (∼665 µm × 665 µm) simultaneously. A slightly curved reflection profile was observed due to the variation of the channel width along the horizontal direction. The variation of Δh, however, was less than a few micrometres except near the crystal edge, which could provide a negligible variation of the optical delay. From equations (6) and (8) with the shift Δh = 176 µm at 300 µm far from the edge, the channel width g and the corresponding optical delay $\Delta t_{\rm ph}$ at 10 keV were evaluated to be 90.0 µm and 119 fs, respectively, which agrees well with the design value. The spatial acceptance, defined by the maximum size of the reflected beam, was evaluated to be ∼600 µm (H) × 100 µm (V) by using a larger X-ray beam.

Fig. 3(*b*) shows a rocking curve to be measured. The peak reflectivity reached 67% while the ideal reflectivity was calculated to be 81%. The reduction in reflectivity was associated with residual surface roughness and damage in the illumination area of the crystal. The imperfection of the crystal also produced speckles on the reflected beam, as shown in Fig. 3(*a*). We assumed that the speckles originated from the modulation of phase due to the surface undulation. The phase shift $\Delta\varphi$ caused by the variation in surface height $h_{\rm S}$ is then given by

$$\Delta\phi = \frac{4\pi\delta h_{\rm S}}{\lambda \sin\theta_{\rm B}}, \tag{9}$$

where δ is the deviation from unity of the real part of the refractive index n (= $1 - \delta + i\beta$). Fig. 4(*a*) shows the distribution of phase shift calculated from the surface morphology on the crystal measured with an optical microscope. A large phase shift of $\sim\pi/2$ with high spatial frequencies of ∼65 mm^{-1} could occur within the footprint of the X-ray beam. We consider that this assumption is reasonable because the spatial frequency of the distribution of phase modulation is consistent with that of the speckles. To evaluate the influence of the distorted wavefront on the self-seeding process, we performed an FEL simulation with $E_{\rm e}$ = 7.8 GeV and K = 2.1015 ($E_{\rm ph}$ = 10 keV) under the following simple conditions: (i) a monochromatic seed pulse is produced from a broadband SASE pulse with a bandpass filter located at the exit of the magnetic chicane (without optical delays), (ii) the phase modulation is introduced to the seed pulse after the bandpass filter, (iii) the seed pulse and electron bunch start to interact with each other after propagating through 6 m free space and (iv) the electron bunch is perfectly overlapped with the seed pulse in both time and space when the phase modulation is not introduced. Other parameters were not optimized to focus on the influence of the phase modulation. Fig. 4(*b*) shows a comparison between simulated gain curves with and without the phase modulation. This simulation implies that the distorted wavefront of the seed pulse does not provide serious degradation in the amplification process, possibly because the phase modulation with high spatial frequencies is smeared while propagating

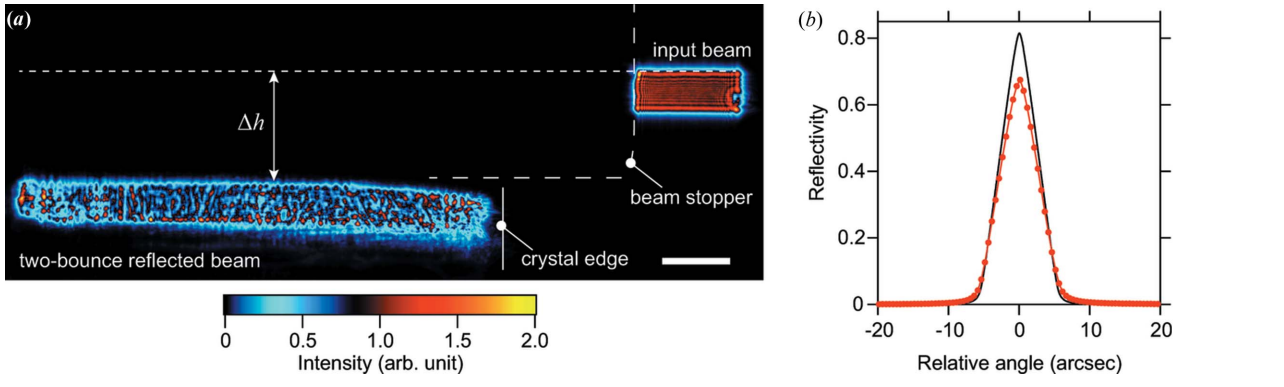

Figure 3
(*a*) Measured two-bounce reflection profile from a micro channel-cut crystal under the exact Bragg condition. This image is created by combining some images taken at several crystal positions. The upper-right beam is the incident beam propagating out of the crystal and beam stopper. The location of the beam stopper and the crystal edge is displayed as a long-dashed line and a solid line, respectively. Scale bar shows 100 µm. (*b*) Rocking curves measured (circles) and calculated (solid line).

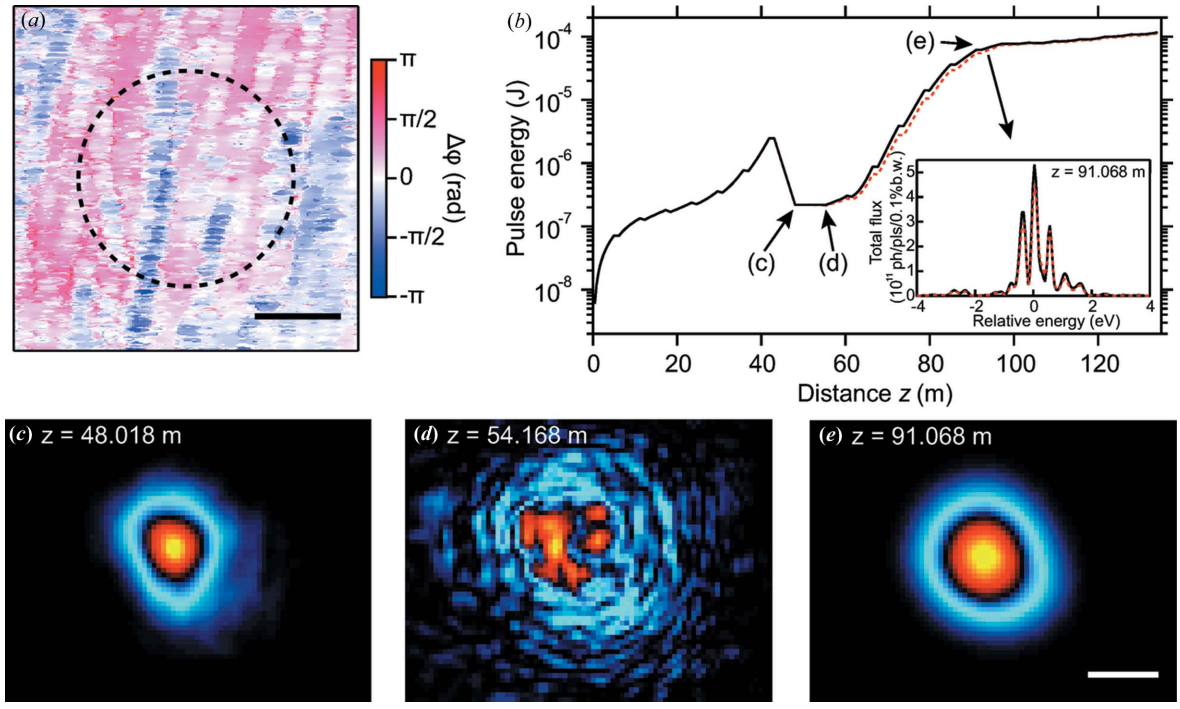

Figure 4
(*a*) Distribution of phase shift converted from the surface morphology on the crystal measured with an optical microscope. The dashed circle shows an expected footprint of the XFEL beam with a diameter of 50 µm. Scale bar represents 20 µm. (*b*) Simulated gain curves in the reflection self-seeding using a seed without (solid line) and with (dashed line) the phase modulation. The electron beam energy is 7.8 GeV with $K = 2.1015$ ($E_{ph} = 10$ keV). The inset of (*b*) shows an example of the spectrum at a distance $z = 91.1$ m. Spatial profiles of the XFEL beam at (*c*) $z = 48.0$ m (just downstream of the bandpass filter), (*d*) $z = 54.2$ m, where the seed pulse starts interacting with the electron bunch, and (*e*) $z = 91.1$ m. Scale bar represents 50 µm.

through the second undulator section, and the TEM_{00} spatial mode in the seed pulse is preferentially amplified. Note that this simulation did not take into account the reduction in peak reflectivity, which could decrease the spectral brightness of the seed and the resultant seeded XFEL beam while providing a similar trend of the gain curve to this simulation.

4. Feasibility test at SACLA

We tested the micro channel-cut monochromator at BL3 of SACLA (Tono *et al.*, 2017) in which 21 undulator modules (U1–U21) are implemented. The magnetic chicane with a length of 5.1 m is placed between U8 and U9. A SASE XFEL beam needed for producing a monochromatic seed was generated with five undulator modules (U4–U8) in the first undulator section. The averaged power of the SASE XFEL beam was estimated to be 4.8 GW (48 µJ within a 10 fs pulse width) at 10 keV with a bandwidth of ∼30 eV in FWHM. The micro channel-cut monochromator was placed at the middle of the magnetic chicane. The size of the SASE beam in the monochromator was evaluated to be ∼65 µm (H) × 45 µm (V) in FWHM through knife-edge scans with the beam stopper, which was consistent with the results of the FEL simulation. Fig. 5 displays the averaged spectrum of the seed without amplification in the second undulator section measured by scanning a speckle-free Si(220) channel-cut crystal (Hirano *et al.*, 2016), placed in experimental hutch 2, 167 m downstream of the monochromator. The spectrum shows a nearly ideal bandwidth of ∼1 eV in FWHM without broadband background, indicating that the crystal successfully produced a seed beam while removing the transmitted SASE beam. With the power of the seed of ∼88 MW (0.88 µJ, 10 fs), the conversion efficiency was experimentally estimated to be 2×10^{-2}, which is ∼10 times higher than the theoretical

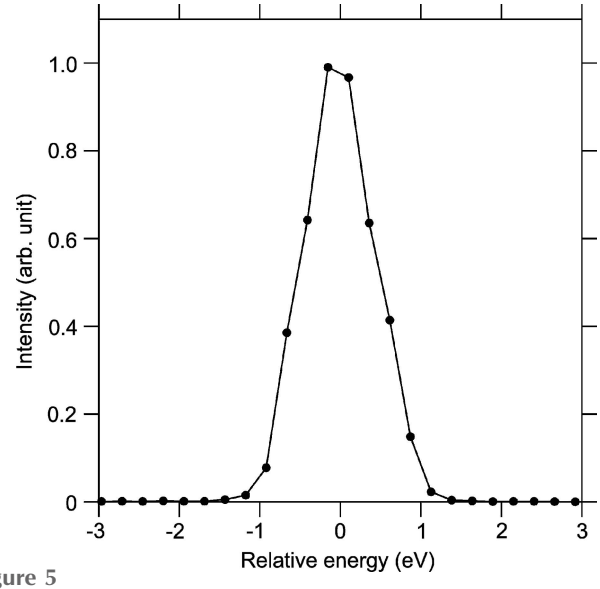

Figure 5
Averaged spectrum of the seed measured with a Si(220) channel-cut crystal. The number of accumulation at each point is 100 shots. The central photon energy is 10 keV.

efficiency of the transmission monochromator with a diamond (400) crystal. Note that the relative bandwidth of the seed produced with the Si(111) micro channel-cut monochromator, 1.3×10^{-4}, was approximately three times wider than that with the diamond (400) monochromator, which primarily contributes to the increase of the conversion efficiency. However, this result suggests that the efficiency for reflection-based monochromators used in this study could be higher than that for transmission-based monochromators even if the seed bandwidths are identical.

5. Conclusions and future perspectives

In conclusion, we have developed a micro channel-cut Si(111) crystal monochromator for self-seeding in hard X-ray FELs. The channel width was evaluated to be 90.0 µm, which gives an optical delay of 119 fs to a 10 keV seed pulse. A clean seed beam without broadband background in the spectrum was obtained through the micro channel-cut monochromator at BL3 of SACLA. An unprecedented high conversion efficiency from a broadband SASE beam to a seed of 2×10^{-2} was experimentally confirmed, allowing one to use an original SASE beam at moderate intensities and, therefore, a high-quality electron bunch can be used for amplification of the seed.

Although the clean and intense seed pulse to be available with the micro channel-cut monochromator and the resultant high-quality electron bunch should increase the spectral brightness of seeded XFELs, further enhancement of spectral brightness will be achieved if the surface quality of the crystal is improved. Chemical etching with atmospheric pressure plasma employed for fabrication of speckle-free crystal optics (Osaka *et al.*, 2013; Hirano *et al.*, 2016), called plasma chemical vaporization machining (PCVM) (Mori *et al.*, 2000), is a promising approach for this purpose. Furthermore, a seeded XFEL beam generated with the micro channel-cut monochromator using the Si(111) diffraction will not be fully coherent in time because the bandwidth of the seed (∼1 eV) is wider than the typical spike width of the SASE beam (∼0.4 eV) (Inubushi *et al.*, 2012, 2017; Osaka *et al.*, 2017). Generation of fully coherent XFEL pulses could be realized by using a high-order diffraction of which the bandwidth is narrower than the spike width. Achieving fabrication of the speckle-free micro channel-cut crystal through the PCVM technique allows one to use a high-order diffraction with nearly ideal conversion efficiency and spectral brightness of the seed, which should pave the way to realization of fully coherent XFELs with high intensities.

Acknowledgements

The authors would like to thank the staff of SPring-8 and SACLA facilities for their continuous support. We would also like to thank Dr Y. Kohmura for his support in the characterization of the micro channel-cut crystal at BL29XU of SPring-8, and Drs T. Hara, T. Inagaki, H. Ohashi and Y. Inubushi for their help in installing the monochromator to BL3 of SACLA. We are grateful for the valuable advice from Drs H. Tanaka, S. Goto, K. Tamasaku, T. Tanaka, K. Togawa, K. Tono and T. Ishikawa.

Funding information

The following funding is acknowledged: Special Postdoctral Researcher Program of RIKEN; JSPS KAKENHI (grant No. 18K18307). The characterization of the crystal was carried out with the approval of RIKEN (Proposal Nos. 20170003 and 20180061.

References

Amann, J., Berg, W., Blank, V., Decker, F.-J., Ding, Y., Emma, P., Feng, Y., Frisch, J., Fritz, D., Hastings, J., Huang, Z., Krzywinski, J., Lindberg, R., Loos, H., Lutman, A., Nuhn, H.-D., Ratner, D., Rzepiela, J., Shu, D., Shvyd'ko, Yu., Spampinati, S., Stoupin, S., Terentyev, S., Trakhtenberg, E., Walz, D., Welch, J., Wu, J., Zholents, A. & Zhu, D. (2012). *Nat. Photon.* **6**, 693–698.

Bonifacio, R., Pellegrini, C. & Narducci, L. M. (1984). *Opt. Commun.* **50**, 373–378.

Bonse, U. & Hart, M. (1965). *Appl. Phys. Lett.* **7**, 238–240.

Diaz, A., Mocuta, C., Stangl, J., Keplinger, M., Weitkamp, T., Pfeiffer, F., David, C., Metzger, T. H. & Bauer, G. (2010). *J. Synchrotron Rad.* **17**, 299–307.

Emma, P., Akre, R., Arthur, J., Bionta, R., Bostedt, C., Bozek, J., Brachmann, A., Bucksbaum, P., Coffee, R., Decker, F.-J., Ding, Y., Dowell, D., Edstrom, S., Fisher, A., Frisch, J., Gilevich, S., Hastings, J., Hays, G., Hering, Ph., Huang, Z., Iverson, R., Loos, H., Messerschmidt, M., Miahnahri, A., Moeller, S., Nuhn, H.-D., Pile, G., Ratner, D., Rzepiela, J., Schultz, D., Smith, T., Stefan, P., Tompkins, H., Turner, J., Welch, J., White, W., Wu, J., Yocky, G. & Galayda, J. (2010). *Nat. Photon.* **4**, 641–647.

Feldhaus, J., Saldin, E. L., Schneider, J. R., Schneidmiller, E. A. & Yurkov, M. V. (1997). *Opt. Commun.* **140**, 341–352.

Geloni, G., Kocharyan, V. & Saldin, E. L. (2010). *Scheme for Generation of Highly Monochromatic X-rays From a Baseline XFEL Undulator*, DESY Report 10-033. DESY, Hamburg, Germany.

Geloni, G., Kocharyan, V. & Saldin, E. L. (2011). *J. Mod. Opt.* **58**, 1391–1403.

Hara, T., Inubushi, Y., Katayama, T., Sato, T., Tanaka, H., Tanaka, T., Togashi, T., Togawa, K., Tono, K., Yabashi, M. & Ishikawa, T. (2013). *Nat. Commun.* **4**, 2919.

Hirano, T., Osaka, T., Sano, Y., Inubushi, Y., Matsuyama, S., Tono, K., Ishikawa, T., Yabashi, M. & Yamauchi, K. (2016). *Rev. Sci. Instrum.* **87**, 063118.

Huang, Z. & Kim, K.-J. (2007). *Phys. Rev. ST Accel. Beams* **10**, 034801.

Inoue, I., Osaka, T., Hara, T., Tanaka, T., Inagaki, T., Fukui, T., Goto, S., Inubushi, Y., Kimura, H., Kinjo, R., Ohashi, H., Togawa, T., Tono, K., Yamaga, M., Tanaka, H., Ishikawa, T. & Yabashi, M. (2019). *Nat. Photon*, **13**, 319–322.

Inubushi, Y., Inoue, I., Kim, J., Nishihara, A., Matsuyama, S., Yumoto, H., Koyama, T., Tono, K., Ohashi, H., Yamauchi, K. & Yabashi, M. (2017). *Appl. Sci.* **7**, 584.

Inubushi, Y., Tono, K., Togashi, T., Sato, T., Hatsui, T., Kameshima, T., Togawa, K., Hara, T., Tanaka, T., Tanaka, H., Ishikawa, T. & Yabashi, M. (2012). *Phys. Rev. Lett.* **109**, 144801.

Ishikawa, T., Aoyagi, H., Asaka, T., Asano, Y., Azumi, N., Bizen, T., Ego, H., Fukami, K., Fukui, T., Furukawa, Y., Goto, S., Hanaki, H., Hara, T., Hasegawa, T., Hatsui, T., Higashiya, A., Hirono, T., Hosoda, N., Ishii, M., Inagaki, T., Inubushi, Y., Itoga, T., Joti, Y., Kago, M., Kameshima, T., Kimura, H., Kirihara, Y., Kiyomichi, A.,

Kobayashi, T., Kondo, C., Kudo, T., Maesaka, H., Maréchal, X. M., Masuda, T., Matsubara, S., Matsumoto, T., Matsushita, T., Matsui, S., Nagasono, M., Nariyama, N., Ohashi, H., Ohata, T., Ohshima, T., Ono, S., Otake, Y., Saji, C., Sakurai, T., Sato, T., Sawada, K., Seike, T., Shirasawa, K., Sugimoto, T., Suzuki, S., Takahashi, S., Takebe, H., Takeshita, K., Tamasaku, K., Tanaka, H., Tanaka, R., Tanaka, H., Togashi, T., Togawa, K., Tokuhisa, A., Tomizawa, H., Tono, K., Wu, S., Yabashi, M., Yamaga, M., Yamashita, A., Yanagida, K., Zhang, C., Shintake, T., Kitamura, H. & Kumagai, N. (2012). *Nat. Photon.* **6**, 540–544.

Kameshima, T., Takeuchi, A., Uesugi, K., Kudo, T., Kohmura, Y., Tamasaku, K., Muramatsu, K., Yanagitani, T., Yabashi, M. & Hatsui, T. (2019). *Opt. Lett.* **44**, 1403–1406.

Kondratenko, A. M. & Saldin, E. L. (1980). *Part. Accel.* **10**, 207–216.

Lindberg, R. R. & Shvyd'ko, Yu. V. (2012). *Phys. Rev. ST Accel. Beams* **15**, 050706.

Mori, Y., Yamauchi, K., Yamamura, K. & Sano, Y. (2000). *Rev. Sci. Instrum.* **71**, 4627–4632.

Osaka, T., Hirano, T., Morioka, Y., Sano, Y., Inubushi, Y., Togashi, T., Inoue, I., Tono, K., Robert, A., Yamauchi, K., Hastings, J. B. & Yabashi, M. (2017). *IUCrJ*, **4**, 728–733.

Osaka, T., Yabashi, M., Sano, Y., Tono, K., Inubushi, Y., Sato, T., Matsuyama, S., Ishikawa, T. & Yamauchi, K. (2013). *Opt. Express*, **21**, 2823–2831.

Saldin, E. L., Schneidmiller, E. A. & Yurkov, M. V. (1999). *The Physics of Free Electron Lasers*. Berlin: Springer.

Tamasaku, K., Tanaka, Y., Yabashi, M., Yamazaki, H., Kawamura, N., Suzuki, M. & Ishikawa, T. (2001). *Nucl. Instrum. Methods Phys. Res. A*, **467–468**, 686–689.

Tanaka, T. (2015). *J. Synchrotron Rad.* **22**, 1319–1326.

Tono, K., Togashi, T., Inubushi, Y., Katayama, T., Owada, S., Yabuuchi, T., Kon, A., Inoue, I., Osaka, T., Yumoto, H., Koyama, T., Ohashi, H. & Yabashi, M. (2017). *Proc. SPIE*, **10237**, 1023706.

Yabashi, M., Yamazaki, H., Tamasaku, K., Goto, S., Takeshita, K., Mochizuki, T., Yoneda, Y., Furukawa, Y. & Ishikawa, T. (1999). *Proc. SPIE*, **3773**, 2.